Viscoelastic flow simulations in model porous media

De, S.; Kuipers, J.A.M.; Peters, E.A.J.F.; Padding, Johan

DOI
10.1103/PhysRevFluids.2.053303

Publication date
2017

Document Version
Final published version

Published in
Physical Review Fluids

Viscoelastic flow simulations in model porous media

S. De, J. A. M. Kuipers, E. A. J. F. Peters, and J. T. Padding*
Department of Chemical Engineering and Chemistry, Eindhoven University of Technology, 5612 AZ Eindhoven, Netherlands
(Received 5 September 2016; published 15 May 2017)

We investigate the flow of unsteadfy three-dimensional viscoelastic fluid through an array of symmetric and asymmetric sets of cylinders constituting a model porous medium. The simulations are performed using a finite-volume methodology with a staggered grid. The solid-fluid interfaces of the porous structure are modeled using a second-order immersed boundary method [S. De *et al.*, J. Non-Newtonian Fluid Mech. **232**, 67 (2016)]. A finitely extensible nonlinear elastic constitutive model with Peterlin closure is used to model the viscoelastic part. By means of periodic boundary conditions, we model the flow behavior for a Newtonian as well as a viscoelastic fluid through successive contractions and expansions. We observe the presence of counterrotating vortices in the dead ends of our geometry. The simulations provide detailed insight into how flow structure, viscoelastic stresses, and viscoelastic work change with increasing Deborah number De. We observe completely different flow structures and different distributions of the viscoelastic work at high De in the symmetric and asymmetric configurations, even though they have the exact same porosity. Moreover, we find that even for the symmetric contraction-expansion flow, most energy dissipation is occurring in shear-dominated regions of the flow domain, not in extensional-flow-dominated regions.

DOI: 10.1103/PhysRevFluids.2.053303

I. INTRODUCTION

Viscoelastic fluids exhibit more complex flow features in porous media compared to their Newtonian counterpart. Research in the field of viscoelastic fluids has attained considerable attention due to its very important industrial applications, such as enhanced oil recovery, polymer extrusion, food processing, and biological flows [1].

Experimentally, a great deal of effort has been made to understand the complex flow of viscoelastic fluids through porous media. Usually packed beds and rock cores are used as a tool to study the pressure drop and flow characteristics of viscoelastic fluids [2–4]. Undulating channels, channels with obstacles, and microfluidic devices have been used to study the flow of polymeric fluid in a controlled and simplified manner [5–9].

Numerical investigation of Newtonian fluids flowing at low Reynolds number through porous media is well established [1] and can be approximated using Darcy's law. On the contrary, due to the complex interplay of fluid rheology and pore structure, the flow of viscoelastic fluid through a porous medium is far from being fully understood. In the literature several different classes of numerical models exist to simulate a porous medium for non-Newtonian fluids, namely, continuum models based on the generalized Darcy principle [10], pore network models [11], and direct numerical simulations based on computational fluid dynamics on the pore scale. Though direct numerical simulations on the pore scale can predict exact flow features of a viscoelastic fluid through a representative porous medium, they are limited due to the high computational costs and convergence issues in a three-dimensional framework. Previously, many researchers have investigated numerically the flow of viscoelastic fluids through simple porous media using both finite-element and

*Present address: Process & Energy Department, Delft University of Technology, 2628 CD Delft, Netherlands; Corresponding author: J.T.Padding@tudelft.nl

finite-volume methods [12–15]. The viscoelastic fluid flow through a periodic array of cylinders and the effects of permeability were studied by Alcocer and Singh [16]. Morais *et al.* [17] used direct numerical simulations to study flow of power-law fluids through a disordered porous medium. Gillissen [18] studied the shear and extensional effects for viscoelastic fluid flow through a model pore geometry. Grill *et al.* [19] studied the flow of viscoelastic fluid through a periodic array of cylindrical objects. Both experiments and simulations show the presence of an elastic instability and subsequent increase in pressure drop at high viscoelasticity [20–22]. The onset of elastic instabilities for complex flow structures and the effects of curved streamlines are also reported [23]. The concept of elastic turbulence in relation to elastic instabilities for polymeric flow has been shown by Groisman and Steinberg [24,25]. Elastic instabilities in a Taylor-Couette and Taylor-Dean flows have also been studied in detail [26,27]. The review paper of Larson [28] describes the theory and experimental work on elastic instabilities for different types of applications. A flow pattern transition, from a stable symmetric to an asymmetric flow due to elastic instability effects, was also studied [29].

In this study we use a coupled finite-volume–immersed boundary method approach to model the viscoelastic fluid flow in a model porous medium. The implementation of the method was thoroughly discussed in our earlier work [30]. In the present paper we create two idealized model pore structures: one with a symmetric and another with an asymmetric periodic arrangement of cylindrical objects. Both structures have the same porosity, but due to the difference in geometry the deformation rates are different in the flow domain. We will show how velocity streamlines and non-Newtonian stresses develop in the two different flow domains with increasing viscoelasticity. We will perform a thorough analysis of flow topology and energy dissipation rates, which provides detailed insight into the shear and extensional effects of viscoelastic fluids in a porous structure. The simulations reveal that for viscoelastic fluids the pore configuration plays a very important role, leading to completely different flow structures even at the same porosity.

II. GOVERNING EQUATIONS

A. Constitutive equations

The fundamental equations for an isothermal incompressible viscoelastic flow are the continuity equation, momentum equation, and a constitutive equation for the non-Newtonian stress components. The first two are as follows:

$$\nabla \cdot \mathbf{u} = 0, \tag{1}$$

$$\rho\left[\frac{\partial \mathbf{u}}{\partial t} + \mathbf{u} \cdot \nabla \mathbf{u}\right] = -\nabla p + 2\eta_s \nabla \cdot \mathbf{D} + \nabla \cdot \boldsymbol{\tau}. \tag{2}$$

Here $\mathbf{u}$ is the velocity vector, ρ is the fluid density (assumed to be constant), p is the pressure, and $\boldsymbol{\tau}$ is the viscoelastic stress tensor. The Newtonian solvent contribution is explicitly added to the stress and defined as $2\eta_s\mathbf{D}$, where the rate of deformation is $\mathbf{D} = [\nabla\mathbf{u} + (\nabla\mathbf{u})^T]/2$. The solvent viscosity η_s is assumed to be constant. In this work the viscoelastic stress is modeled through the constitutive finitely extensible nonlinear elastic constitutive model with Peterlin closure (the FENE-P model), which is based on the finitely extensible nonlinear elastic dumbbell for polymeric materials, as explained in detail by Bird *et al.* [31,32]. The equation is derived from molecular theory, where a polymer chain is represented as a dumbbell consisting of two beads connected by a spring. Other basic rheological models, such as the Maxwell model and Oldroyd-B model, take the elastic force between the beads to be proportional to the separation between the beads. These types of models have the disadvantage that the dumbbells can be stretched indefinitely, leading to divergent behavior and numerical instabilities in strong extensional flow. To overcome this problem, a finitely extensible spring is implemented. For problems with high strain rates, a FENE-P model provides bounded solutions, while constitutive models based on linear springs, such as the Oldroyd-B model, may give divergent solutions. The FENE-P model has been used in many previous studies for viscoelastic

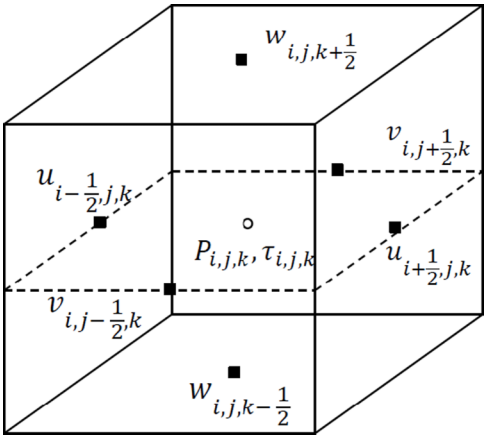

FIG. 1. Location of primitive variables in a three-dimensional control volume (fluid cell).

flow simulations. The basic form of the FENE-P constitutive equation is

$$f(\boldsymbol{\tau})\boldsymbol{\tau} + \lambda \overset{\nabla}{\boldsymbol{\tau}} = 2a\eta_p \mathbf{D}, \tag{3}$$

with $f(\boldsymbol{\tau}) = 1 + \frac{3a+(\lambda/\eta_p)\mathrm{tr}(\boldsymbol{\tau})}{L^2}$ and $a = \frac{L^2}{L^2-3}$. In Eq. (3) the operator ∇ (above a second-rank tensor) represents the upper convected time derivative, defined as

$$\overset{\nabla}{\boldsymbol{\tau}} = \frac{\partial \boldsymbol{\tau}}{\partial t} + \mathbf{u}\cdot\nabla\boldsymbol{\tau} - \nabla\mathbf{u}^T\cdot\boldsymbol{\tau} - \boldsymbol{\tau}\cdot\nabla\mathbf{u}. \tag{4}$$

In Eq. (3) the constant λ is the dominant relaxation time of the polymer, η_p is the zero-shear rate polymer viscosity, $\mathrm{tr}(\boldsymbol{\tau})$ denotes the trace of the stress tensor, and L characterizes the maximum polymer extensibility. This parameter equals the maximum length of a FENE dumbbell and is normalized with the equilibrium length of the limiting linear spring described as $\sqrt{k_B T/K}$, where T is the absolute temperature, k_B is Boltzmann's constant, and K is the Hookean spring constant for an entropic spring. When $L^2 \to \infty$ the Oldroyd-B model is recovered. Equation (4) represents the upper convected time derivative of the viscoelastic stress term, which is coupled with the Navier-Stokes equation. The total zero-shear rate viscosity of the polymer solution is given as $\eta = \eta_s + \eta_p$. The viscosity ratio, which is a measure of polymer concentration, is defined as $\beta = \eta_s/\eta$.

We simulate an unsteady viscoelastic flow through an array of symmetric and asymmetric cylinders constituting a model porous medium by using computational fluid dynamics. The primitive variables used in the formulation of the model are velocity, pressure, and polymer stress. All the mass and momentum equations are considered and discretized in space and time. A coupled finite-volume–immersed boundary methodology [30] with a staggered grid is applied. In the finite-volume method, the computational domain is divided into small control volumes ΔV and the primitive variables are solved in the control volumes in an integral form over a time interval Δt.

The location of all the primitive variables in a three-dimensional cell are indicated in Fig. 1. The velocity components u, v, and w are located at the faces, while pressure p and stress $\boldsymbol{\tau}$ variables are located at the center of the cubic cell.

The viscoelastic phase equations are solved in three dimensions on a Cartesian staggered grid. We apply the discrete elastic viscous stress splitting scheme, originally proposed by Guénette and Fortin [33], to introduce the viscoelastic stress terms in the Navier-Stokes equation because it stabilizes the momentum equation, which is especially important at larger polymer stresses occurring at small β and/or higher Deborah numbers. A uniform grid spacing is used in all directions. The temporal

discretization for the momentum equation is

$$\rho \mathbf{u}^{n+1} = \rho \mathbf{u}^n + \Delta t \left\{ -\nabla p^{n+1} - \left[\mathbf{C}_f^{n+1} + \left(\mathbf{C}_m^n - \mathbf{C}_f^n \right) \right] + \left[(\eta_s + \eta_p) \nabla^2 \mathbf{u}^{n+1} + \nabla \cdot \boldsymbol{\tau}^n \right] + \rho \mathbf{g} - \mathbf{E}_p^n \right\}. \tag{5}$$

Here $\eta_p \nabla^2 \mathbf{u}^{n+1}$ and $\mathbf{E}_p^n = \eta_p \nabla^2 \mathbf{u}^n$ are the extra variables we introduce to obtain numerical stability, n indicates the time index, and $\mathbf{C}$ represents the net convective momentum flux given by

$$\mathbf{C} = \rho(\nabla \cdot \mathbf{uu}). \tag{6}$$

In the calculation of the convective term a deferred correction method is implemented. Here the first-order upwind scheme is used for the implicit evaluation of the convection term (called $\mathbf{C}_f$). The deferred correction contribution that is used to achieve second-order spatial accuracy while maintaining stability is $\mathbf{C}_m^n - \mathbf{C}_f^n$ and is treated explicitly. In this expression $\mathbf{C}_m$ indicates the convective term evaluated by the total variation diminishing (TVD) minmod scheme. A second-order central-difference scheme is used for the discretization of diffusive terms.

In Eq. (5) the viscoelastic stress part $\boldsymbol{\tau}$ is calculated by solving Eq. (3). The viscoelastic stress tensors are all located in the center of a fluid cell and interpolated appropriately during the velocity updates. The convective part of Eq. (3) is solved by using the second-order minmod TVD scheme with deferred correction.

Equation (5) is solved by a fractional step method, where the tentative velocity field in the first step is computed from

$$\rho \mathbf{u}^{**} = \rho \mathbf{u}^n + \Delta t \left\{ -\nabla p^{n+1} - \left[\mathbf{C}_f^{**} + \left(\mathbf{C}_m^n - \mathbf{C}_f^n \right) \right] + \left[(\eta_s + \eta_p) \nabla^2 \mathbf{u}^{**} + \nabla \cdot \boldsymbol{\tau}^n \right] + \rho \mathbf{g} - \mathbf{E}_p^n \right\}. \tag{7}$$

In Eq. (7) we need to solve a set of linear equations. The enforcement of a no-slip boundary condition at the surface of the immersed boundaries is handled at the level of the discretized momentum equations by our immersed boundary methodology. We solve the resulting sparse matrix for each velocity component in a parallel computational environment. The velocity at the new time step $n + 1$ is related to the tentative velocity as follows:

$$\mathbf{u}^{n+1} = \mathbf{u}^{**} - \frac{\Delta t}{\rho} \nabla(\delta p), \tag{8}$$

where $\delta p = p^{n+1} - p^n$ is the pressure correction. As $\mathbf{u}^{n+1}$ should satisfy the equation of continuity, the pressure Poisson equation is calculated as

$$\nabla \cdot \left\{ \frac{\Delta t}{\rho} \nabla(\delta p) \right\} = \nabla \cdot \mathbf{u}^{**}. \tag{9}$$

This is again solved using the BICCG solver. We use a robust and efficient block-incomplete Cholesky conjugate gradient (BICCG) algorithm for solving the resulting sparse matrix for each velocity component in a parallel computational environment [30]. The solver iterations are performed until the norm of the residual matrix is less than the convergence criterion, which is set at 10^{-14} for our simulations. As the viscoelastic stress tensor components are coupled among themselves and with the momentum equation, the velocity at the new time level $\mathbf{u}^{n+1}$ is used to calculate the stress value accordingly.

As a steady-state criterion, the relative change of velocity and stress components between two subsequent time steps is computed in all the cells in a longer time range. If the magnitude of the relative change is less than 10^{-4} the simulation is stopped.

The main advantage of using an immersed boundary method for the coupling to the walls is that the no-slip boundary conditions are enforced at the level of the discretized momentum equations of the fluid, by extrapolating the velocity field along each Cartesian direction towards the body surface using a second-order polynomial. Thus no remeshing is required at the fluid solid interface and the method is computationally robust and cheaper.

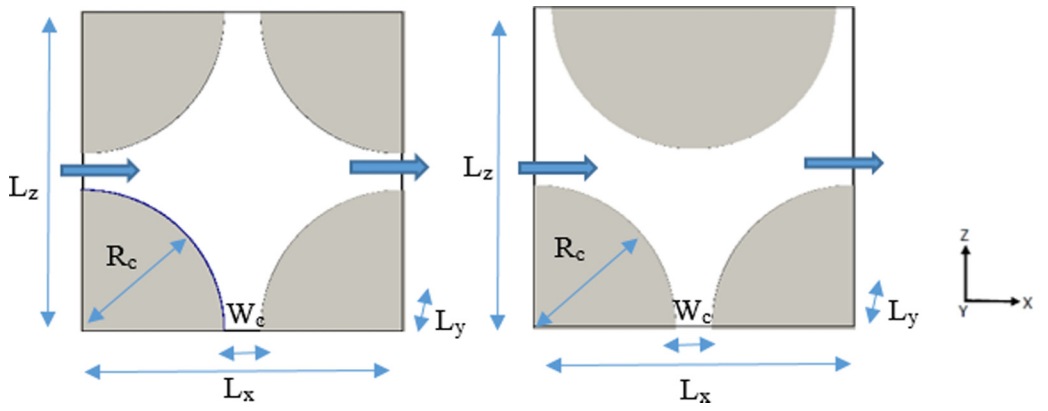

FIG. 2. Two-dimensional view of the symmetric (left) and asymmetric (right) geometry configurations. Thick arrows indicate the dominant flow direction. Walls are present at the top and bottom z boundaries to create dead ends.

B. Problem description

We apply our method to investigate viscoelastic flow through porous media constituting symmetric and asymmetric arrays of cylindrical objects arranged in a periodic manner (Fig. 2). Both configurations have a porosity ε of 0.38. Such an arrangement forces the viscoelastic fluid to continuously undergo successive contraction and expansion. We expect that in some cases the polymer stresses due to extensional deformations can become of similar importance as stresses caused by shear deformation. The interesting part of these simulations is that the symmetric and asymmetric arrangements of cylinders can be thought to constitute two extreme configurations of an ideal porous medium. In the symmetric configuration along the centerline, in a frame of reference that comoves with the flow, the flow is almost purely extensional, while in the asymmetric geometry the deformation is expected to be shear dominated almost everywhere. All porous media are expected to have a combination of these two flow patterns (i.e., extension and shear).

In all simulations the main flow direction is along the x axis. To model successive contractions and expansions a periodic boundary condition is implemented in the flow direction (x) and in the direction of the cylinder axes (y). Along the third (z) direction a no-slip boundary condition is implemented, giving rise to a dead end in between two cylinders. The dimensions of the geometry are $L_x = 2.25R_c, L_y = 0.0625R_c$, and $L_z = 2.25R_c$, where L_x, L_y, and L_z are the domain sizes along the x, y, and z directions, respectively, and R_c is the cylinder radius, taken to be the unit length scale in our simulations. The gap width between two consecutive cylinders in the flow direction (x) is $W_c = 0.25R_c$. The flow is driven by a constant body force exerted on the fluid in the x direction.

We simulate both a Newtonian fluid and a FENE-P viscoelastic fluid, as described in Sec. II. We use a constant extensional parameter L^2 of 100. The viscosity ratio β is kept at 0.33. In all our simulations we keep the Reynolds number at a low value of 0.01, ensuring that we are always in the creeping flow regime and any type of inertial effects will be insignificant. The amount of viscoelasticity is characterized by the Deborah number defined as $\mathrm{De} = \lambda U/R_c$, based on the cylinder radius and mean flow velocity U. In our work De is increased from 0 to 6 by increasing the relaxation time λ while using a constant body force to drive the flow, which is equivalent to applying a constant pressure drop across the domain. To quantify the measured stresses in a dimensionless manner, we will nondimensionalize them as $\tau_{\alpha\beta_n} = \frac{\tau_{\alpha\beta}}{\eta U/R_c}$.

We have performed simulations for two different mesh sizes of $\Delta = R_c/96$ and $\Delta = R_c/120$. The results for $\Delta = R_c/96$ and $\Delta = R_c/120$ were virtually indistinguishable, even at $\mathrm{De} > 1$ (not shown). Thus all results in the remainder of this paper are based on the mesh size $\Delta = R_c/96$. It should be noted that we needed to keep the Courant-Friedrichs-Lewy number lower than 0.01 in all

our simulations, leading to considerable computational costs. At De < 1 a larger time step can be utilized, but at De $\geqslant 1$, a small time step is required for smooth convergence.

We have employed a single periodic cell for our simulations. We have also compared our results with two and three periodic unit cells in the flow directions and found no difference on the viscoelastic stress and velocity profiles well beyond the onset of elastic instability, as compared to a single periodic cell. A similar type of periodic boundary condition implementation for the study of viscoelastic flow is well documented in the literature [6,12,19]. We warn that at much larger De (greater than 6.0) than studied here, the use of periodic boundary conditions becomes questionable because the time dependence of the instabilities may vary from one periodic unit cell to another. Having a too small unit cell then leads to a stabilization of the flow. This is true for the system size not only in the flow direction, but also in the two other directions. We leave a more detailed investigation of this influence for flows at higher De to future work.

In the model porous media the polymer undergoes successive contraction and expansion. Due to the continuous interplay of fluid rheology and confining geometry, the precise flow configuration, i.e., the amount of rotational, shear, and extensional flow, will depend on the level of viscoelasticity. To characterize the flow configuration, we introduce a flow topology parameter Q [17], which is the second invariant of the normalized velocity gradient. This parameter is defined as

$$Q = \frac{S^2 - \Omega^2}{S^2 + \Omega^2}, \tag{10}$$

where $S^2 = \frac{1}{2}(S : S)$ and $\Omega^2 = \frac{1}{2}(\Omega : \Omega)$ are invariants of the rate of strain tensor $S = \frac{1}{2}(\nabla \mathbf{u}^T + \nabla \mathbf{u})$ and rate of rotation tensor $\Omega = \frac{1}{2}(\nabla \mathbf{u}^T - \nabla \mathbf{u})$. Values of $Q = -1, 0$, and 1 correspond to pure rotational flow, pure shear flow, and pure elongational flow, respectively.

In this paper we will correlate the above flow topology parameter Q with the amount of energy dissipation in the flow domain. The work performed by the viscoelastic stress per unit volume (in $\mathrm{W/m^3}$) is defined as

$$\dot{E} = \boldsymbol{\tau}_{xx}\frac{\partial u_x}{\partial x} + \boldsymbol{\tau}_{yy}\frac{\partial u_y}{\partial y} + \boldsymbol{\tau}_{zz}\frac{\partial u_z}{\partial z} + \boldsymbol{\tau}_{xy}\left(\frac{\partial u_x}{\partial y} + \frac{\partial u_y}{\partial x}\right) + \boldsymbol{\tau}_{xz}\left(\frac{\partial u_x}{\partial z} + \frac{\partial u_z}{\partial x}\right) + \boldsymbol{\tau}_{yz}\left(\frac{\partial u_y}{\partial z} + \frac{\partial u_z}{\partial y}\right). \tag{11}$$

A detailed study of the topology and the spatial distribution of $\dot{E}$ for the symmetric and asymmetric configurations at different De enables us to understand the flow characteristics of a viscoelastic fluid in the porous media.

To quantify the energy dissipation rate in a dimensionless manner, we express the work performed by viscoelastic stress per unit volume as $E_V = \frac{\dot{E}}{\eta U^2/R_C^2}$. The total energy dissipation rate (viscoelastic plus Newtonian) is also made nondimensional in the same manner and is termed E_t, discussed in detail in Sec. III.

III. NUMERICAL RESULTS

As a reference case, first we study the flow of a Newtonian fluid through the model porous media. Figure 3 shows the velocity streamlines of a Newtonian fluid in the symmetric and asymmetric configurations, colored by the velocity magnitude (normalized by the maximum velocity in the domain). In the symmetric configuration the fluid is forced to flow from a narrow neck to a wide pore area, leading to large differences in velocity magnitude along the centerline. Moreover, the flow streamlines show the presence of slowly moving counterrotating vortices in the dead ends near the no-slip walls.

Similar to the symmetric configuration, in the asymmetric flow the fluid undergoes successive contraction and expansion, but the difference between the maximum and the minimum velocity becomes much smaller and the streamlines are more undulatory. Low-velocity counterrotating vortices are also observed in the dead ends near the no-slip walls in this geometry.

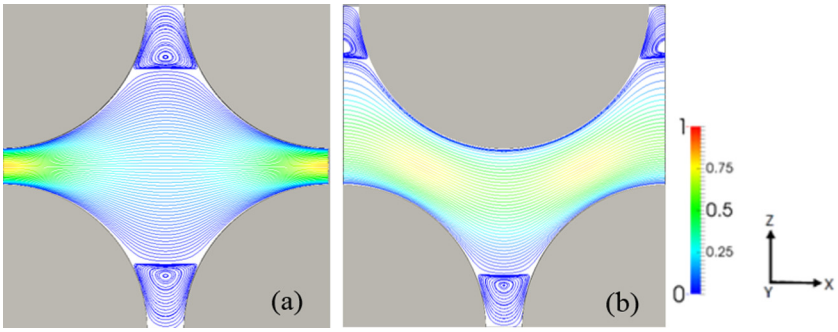

FIG. 3. Velocity streamlines (colored with normalized velocity) for the Newtonian fluid in the (a) symmetric and (b) asymmetric configurations.

Next we study the flow of a non-Newtonian fluid through the model porous media. As shown in Figs. 4 and 5 (snapshots of velocity streamlines, colored with normalized velocity after the same time of simulation), in the range $\mathrm{De} \leqslant 0.1$ the velocity streamlines for viscoelastic fluids are very similar to their Newtonian counterparts, but at higher viscoelasticity, in the range $\mathrm{De} = O(1)$, the streamlines change considerably. The polymer solution undergoes continuous contraction and expansion and shear thins at higher shear rates. The extensional effects also become considerable. Moreover, we observe that the counterrotating vortices become more concave due to elastic effects.

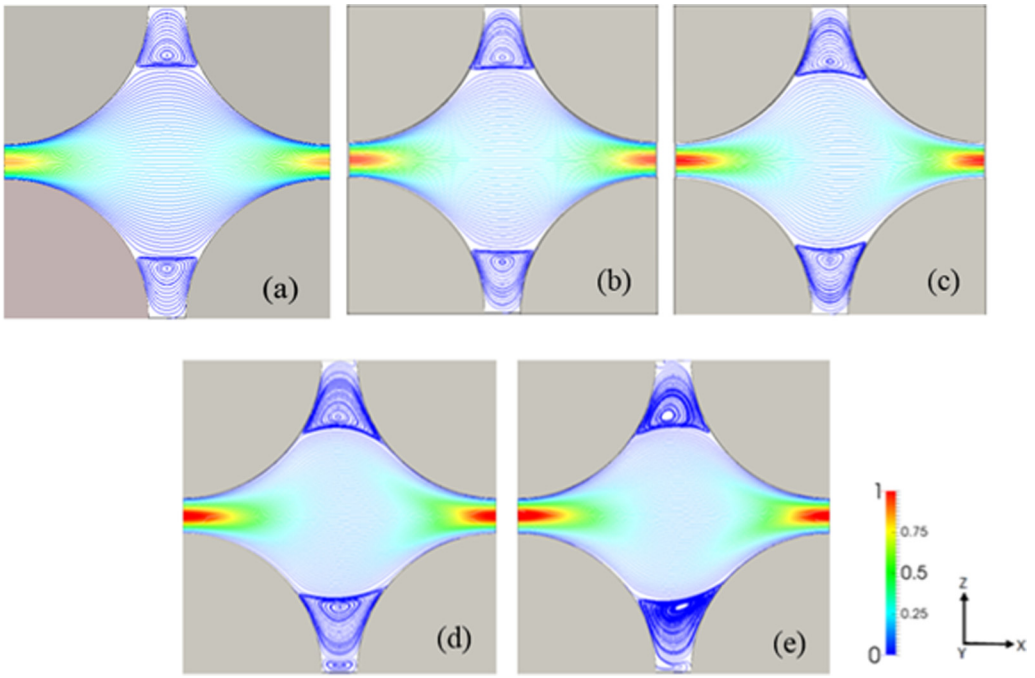

FIG. 4. Streamlines (colored by normalized velocity) for a non-Newtonian fluid flowing at different De through the symmetric configuration: (a) $\mathrm{De} = 0.1$, (b) $\mathrm{De} = 0.5$, (c) $\mathrm{De} = 1.25$, (d) $\mathrm{De} = 2.5$, and (e) $\mathrm{De} = 5.0$. Note that beyond $\mathrm{De} \sim 2$ the streamlines become time dependent and therefore only instantaneous streamlines are shown here.

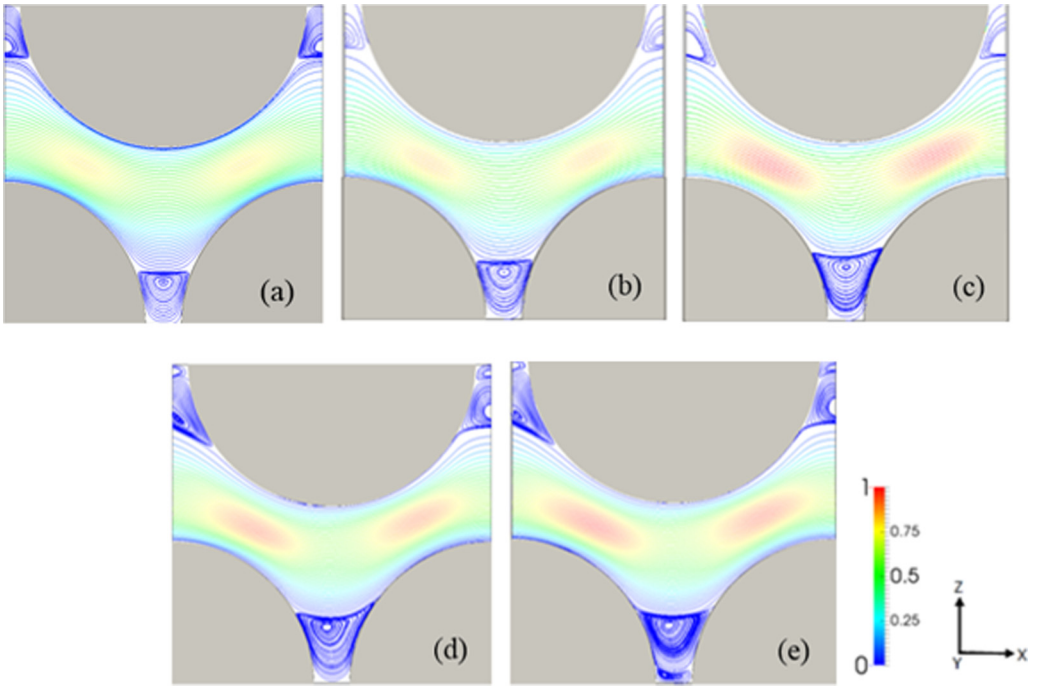

FIG. 5. Streamlines (colored by normalized velocity) for a non-Newtonian fluid flowing at different De through the asymmetric configuration: (a) De = 0.15, (b) De = 0.3, (c) De = 1.5, (d) De = 3.0, and (e) De = 6.0. Note that beyond De $\sim$ 2 the streamlines become time dependent and therefore only instantaneous streamlines are shown here.

The flow profile shows the presence of secondary vortices in the symmetric and asymmetric flow configurations after De $\sim$ 2, which grows further with increased viscoelasticity. Moreover, we can observe that the fore-aft asymmetry becomes stronger and dead zones become more concave in nature. Further, the eyes of the vortices do not align with the symmetry axis. Also, for De $>$ 2 we found that the flow becomes time dependent, which has also been reported by previous researchers [8].

The instantaneous viscoelastic nondimensional normal stress component $\tau_{xx_n} = \frac{\tau_{xx}}{\eta U/R_c}$ along the flow direction is shown in Figs. 6 and 7 for the symmetric and asymmetric configurations, respectively. Such viscoelastic stresses are absent in a Newtonian fluid. We observe that for both configurations the viscoelastic normal stress increases with increasing De, but that the increase is stronger for the asymmetric configuration. This is related to the fact that the largest normal stresses are present near the walls of the cylinders at locations that are shear dominated and more shear is present in the asymmetric configuration, as we will show in detail later in this paper.

The volume-averaged fluid velocity $\langle u \rangle$ in porous media can be controlled by the pressure drop across the sample. According to Darcy's law (12), for a Newtonian fluid the relation between the average pressure gradient $-\frac{dp}{dx}$ and the average fluid velocity through the porous medium is

$$\left(-\frac{dp}{dx}\right) = \frac{\eta \langle u \rangle}{k}. \tag{12}$$

Here k is the permeability, which is related to the pore size distribution and tortuosity of the porous medium itself and η is the viscosity of the fluid. For a viscoelastic fluid, the viscosity is not a constant but generally depends on the flow conditions. However, we can still define an apparent viscosity by using Darcy's law, assuming that the permeability k is constant. Dividing the apparent viscosity

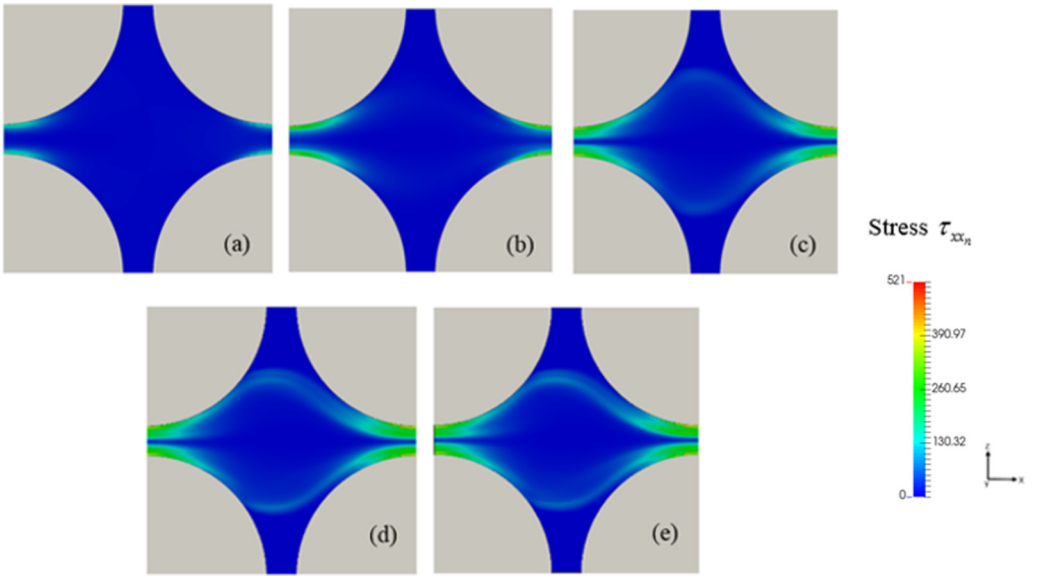

FIG. 6. Instantaneous nondimensional normal stress (τ_{xx_n}) profiles for viscoelastic fluid at different De for the symmetric configuration: (a) De = 0.1, (b) De = 0.5, (c) De = 1.25, (d) De = 2.5, and (e) De = 5.0.

by its low-flow-rate limit gives us insight into the effective flow-induced thinning or thickening of the fluid in the porous medium. In detail, the apparent relative viscosity η_{app} of a viscoelastic fluid flowing with a volumetric flow rate q and pressure drop ΔP through a porous medium is given by

$$\eta_{\text{app}} = \frac{\left(\frac{\Delta P}{q}\right)_{\text{ve}}}{\left(\frac{\Delta P}{q}\right)_{N}}. \tag{13}$$

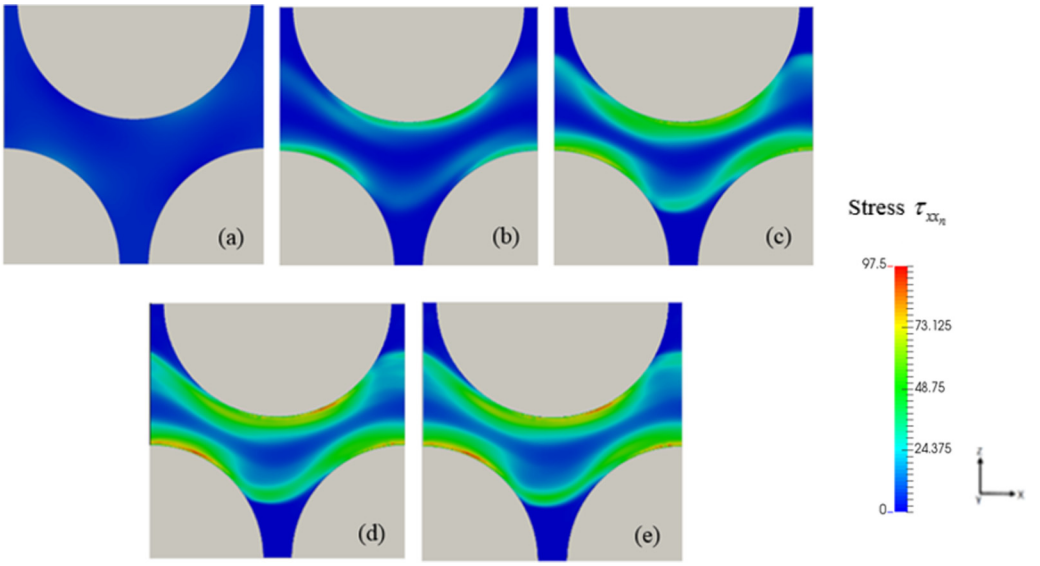

FIG. 7. Instantaneous nondimensional normal stress (τ_{xx_n}) profiles for viscoelastic fluid at different De for the asymmetric configuration: (a) De = 0.15, (b) De = 0.3, (c) De = 1.5, (d) De = 3.0, and (e) De = 6.0.

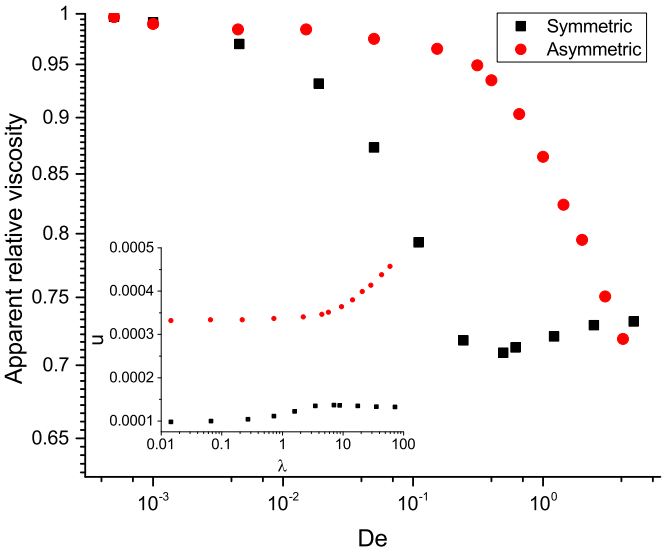

FIG. 8. Apparent relative viscosity versus De for the symmetric and asymmetric configurations.

The subscript ve indicates viscoelastic fluid at a specific flow rate or pressure drop, while the subscript N indicates its Newtonian low-flow-rate or low-pressure drop limit.

Figure 8 depicts how the apparent relative viscosity changes with an increase in viscoelasticity for the symmetric and asymmetric flow configurations. We observe that for the symmetric case the fluid viscosity thins at a much lower De compared to the asymmetric flow structure. This can be attributed to the fact that in the symmetric configuration the fluid needs to undergo a much larger expansion and contraction. This leads to higher thinning effects compared to the asymmetric flow structure at similar shear rates. Because we drive the flow with a constant body force while changing the relaxation time, a change in apparent viscosity corresponds to a change of average velocity for different relaxation times, as shown in the inset of Fig. 8. This behavior matches with the experimental observation of Rosales *et al.* [7]. We also observe an increase in drag in the symmetric configuration after a critical De of 0.5, depicted by an increase in apparent viscosity. These results clearly show that the resistance to flow for a viscoelastic fluid can be very different, depending on the porous geometry, even at the same porosity of the porous medium.

Figure 9 shows the volume-averaged nondimensional normal stress (in the x direction) versus Deborah number for both configurations. The stress initially grows linearly with De, but then levels off to an almost constant value. At higher De the dimensionless normal stress in the symmetric configuration is larger than that in the asymmetric configuration. We will discuss this subsequently.

We will now focus on the flow topology, i.e., how the shear, extensional, and rotational parts of the flow are distributed and develop in the interstitial space. To this end we will visualize the flow topology parameter Q, introduced in Sec. II B, for different De for both the symmetric and asymmetric configurations. As explained $Q = -1, 0$, and 1 correspond to pure rotational, shear, and elongational flows, respectively.

Figure 10 shows the flow topology parameter distribution for the symmetric configuration. We observe highly shear-dominated flow near the cylinder walls and rotation of flow in the dead ends due to the presence of vortices. At very low De we observe a symmetric pattern, as expected for low-Reynolds-number flow of a Newtonian fluid through a symmetric configuration. With increasing De the pattern becomes increasingly asymmetric. Due to the continuous contraction and expansion of the polymeric fluid, we observe that the extensional component becomes increasingly important with increasing De.

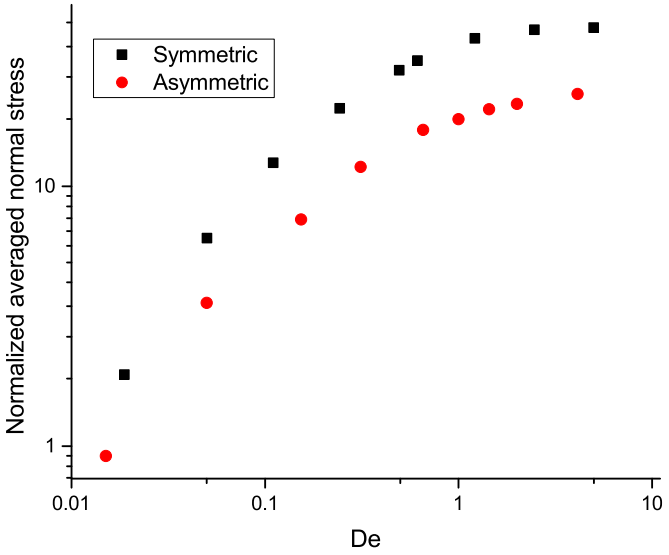

FIG. 9. Volume-averaged dimensionless normal stress versus De for the symmetric and asymmetric configurations.

Figure 11 shows the flow topology parameter distribution for the asymmetric configuration. It is significantly different from the symmetric case. The asymmetric pore network is more dominated by shear flow and slightly less by extensional flow compared to the symmetric structure at similar De.

At De more than approximately 2 we observe that the flow instability changes the overall flow topology. In both the symmetric and asymmetric flow configurations, the onset of a more nonuniform flow topology appears. At higher viscoelasticity the overall contribution of shear starts to dominate. Also in the dead ends, due to the presence of secondary vortices, shear becomes larger and thus the extensional contribution decreases as seen in the asymmetric configuration. This corresponds to the asymmetric velocity streamlines discussed earlier.

The temporal flow instability is shown in Fig. 12. The onset of a time-dependent flow is observed, which breaks the symmetry plane. The time period of oscillation is found to be $\sim 2\lambda$. Figure 12 shows how the flow topology evolves over half a cycle of oscillation. This change of flow topology can be more appreciated in the video in the Supplemental Material [34]. The asymmetric configuration is also found to have similar periodicity (not shown).

To quantify the difference between the symmetric and asymmetric configurations better, histograms of the flow topology parameter are shown in Figs. 13 and 14.

The histogram in Fig. 13 shows that for the symmetric configuration the amount of extensional flow ($Q = 1$) strongly increases beyond De $= 0.1$. There is also a peak near $Q = 0$, signifying shear flow, but it changes only very slightly with increasing De. So we find that for the symmetric flow configuration, with increasing De an increasingly large volume fraction of the polymer solution gets extended due to successive contraction and expansion. It is also observed that at low De the rotational regimes are almost absent due to the symmetric flow profile. Thus the count in the mixed rotation and shear-dominated regime is relatively small compared to higher De (greater than 0.10).

The histogram in Fig. 14 shows that the flow in the asymmetric configuration is indeed much more shear dominated than the flow in the symmetric configuration. The peak near $Q = 0$ also increases with increasing De, while the amount of extensional flow ($Q = 1$) hardly changes. Also, more mixed rotational and shear flow (Q in the range from -0.5 to -0.2) is present in the asymmetric

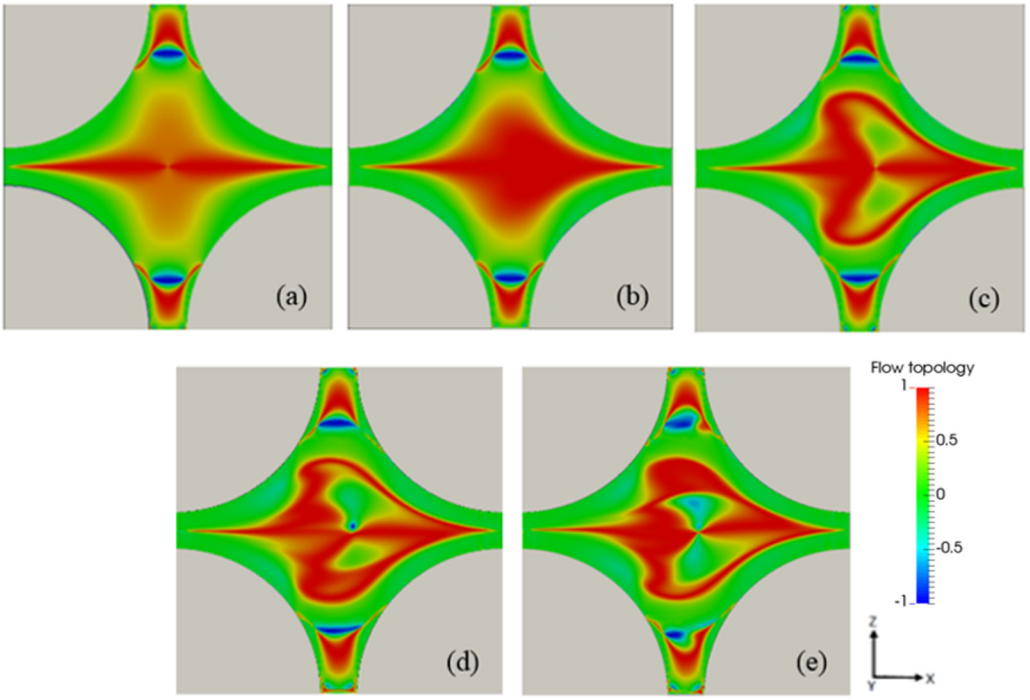

FIG. 10. Instantaneous flow topology parameter at different De for the symmetric configuration: (a) De = 0.1, (b) De = 0.5, (c) De = 1.25, (d) De = 2.5, and (e) De = 5.0.

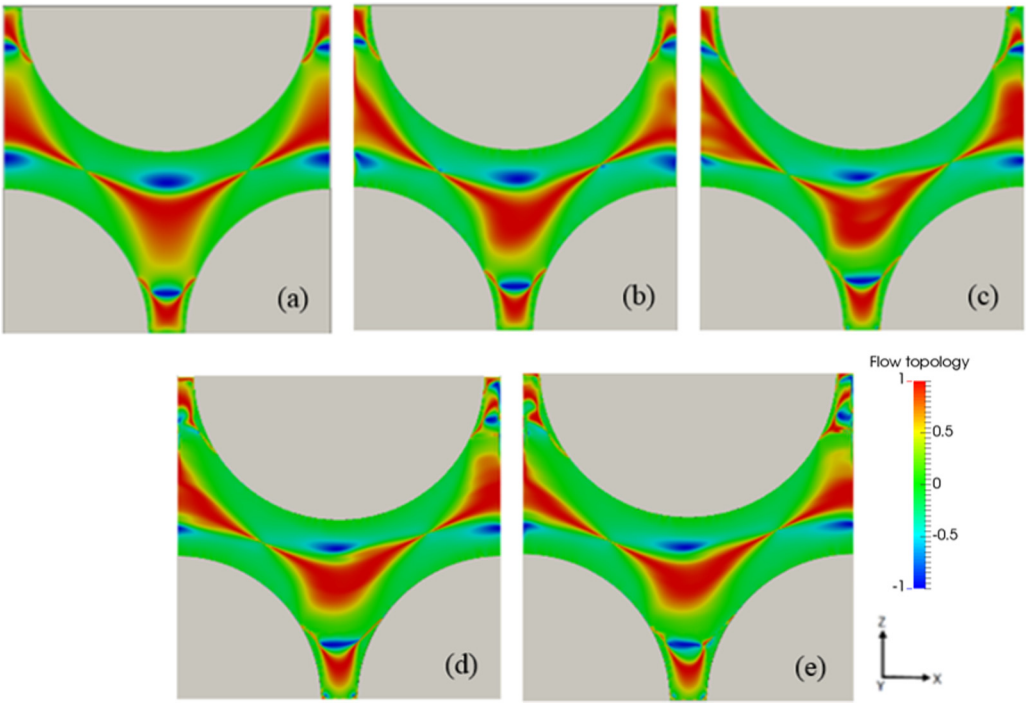

FIG. 11. Instantaneous flow topology parameter at different De for the asymmetric configuration: (a) De = 0.15, (b) De = 0.3, (c) De = 1.5, (d) De = 3.0, and (e) De = 6.0.

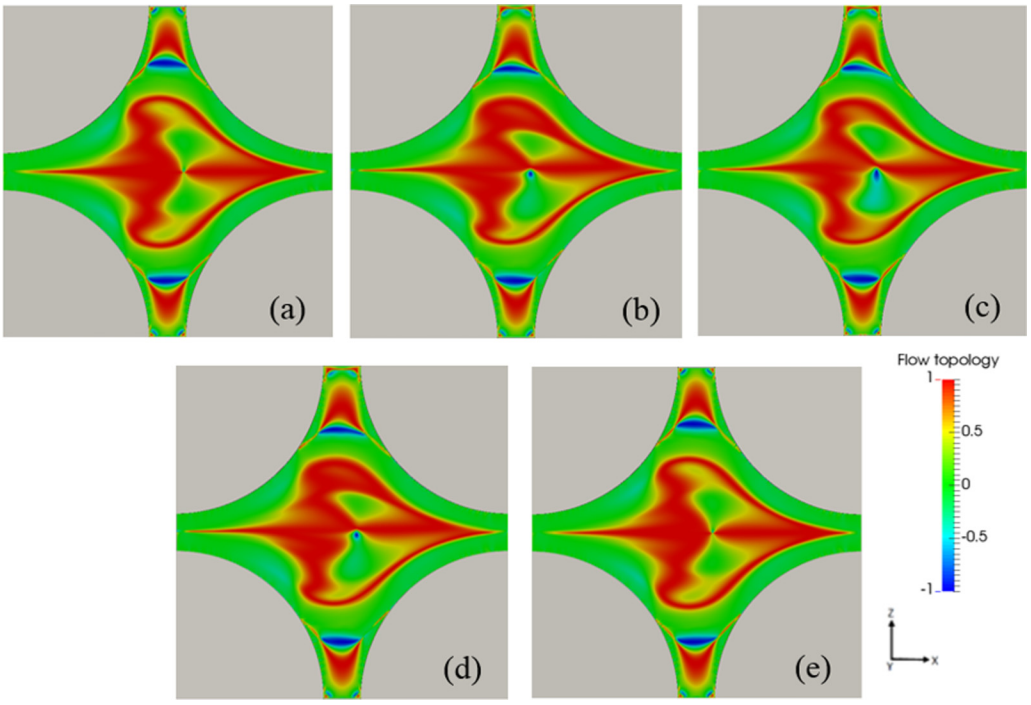

FIG. 12. Snapshots of flow topology parameter for De = 5.0 at different times after flow instability. Half a cycle of oscillation is shown here. A video can be found in the Supplemental Material [34].

configuration. So we find that for the asymmetric flow configuration, a relatively large volume fraction of the polymer solution gets sheared (and rotated) due to contact with the walls.

Next we analyze the spatial distribution of the nondimensional work E_v performed by the viscoelastic stresses per unit volume. The calculation of energy dissipation is described in Sec. II B. Figure 15 shows the spatial distribution of E_v for the symmetric configuration at different De. We have clipped the color scale to clearly show regions in the domain where energy is released by the polymer solution. At all De, energy is dissipated predominantly near the walls in the pore throats. For De of order 1 (or higher), energy is released after the contracting section of the pore throat has ended and farther away from the walls. This is consistent with the physical picture in which polymers in fast contraction flow are extended and therefore store energy in their entropic springs; this energy is subsequently released when the polymers can relax when the contraction flow has stopped.

Figure 16 shows the spatial distribution of E_v for the asymmetric configuration at different De. Clearly, a larger volume fraction of the fluid is dissipating energy at high rates. Moreover, we observe again that at De of order 1 (or higher) the polymers release energy in sections of the domain that have stopped contracting and away from walls.

We will now try to answer the question where most energy is dissipated, in the shear-flo-dominated regions or in the extensional-flow-dominated regions.

Figures 17 and 18 show the dimensionless viscoelastic energy distribution E_V (per unit Q) versus flow topology parameter in the entire flow domain for the symmetric and asymmetric configurations, respectively. The correlation between the flow topology and viscoelastic work can be directly estimated from such analysis. With increased viscoelasticity the flow structure changes. Thus we can determine how the change of flow topology affects the viscoelastic work across the flow domain. For both configurations we observe that most viscoelastic energy is dissipated in shear flow regions with a topology parameter near $Q = 0$, while a much smaller amount of viscoelastic energy is dissipated in the extensional flow regions, even at larger De. So in these contraction-expansion flows

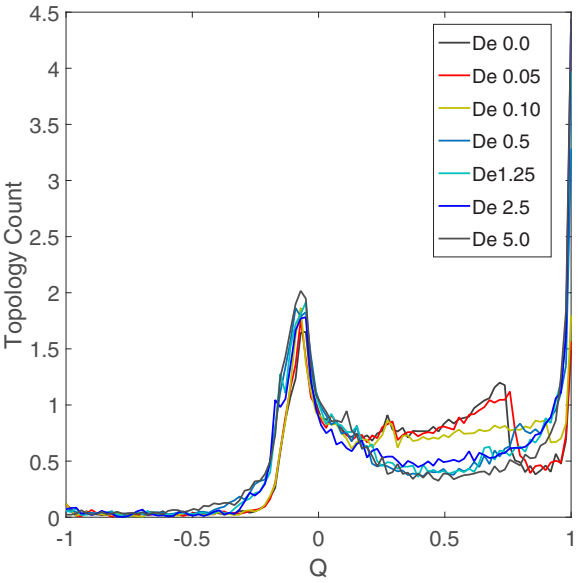

FIG. 13. Flow topology parameter histogram for the symmetric configuration for different De.

most viscoelastic energy dissipation is occurring in the shear flow regions near the walls, not in the extensional flow regions. This is in agreement with recent experimental observations by James *et al.* [35] and Wagner and McKinley [36].

Interestingly, at De of order 1 or higher, viscoelastic energy release (negative dissipation) is occurring near $Q = -0.05$ (almost pure shear flow) for the symmetric configuration, while it is occurring near $Q = -0.35$ (mixed shear and rotational flow) for the asymmetric configuration.

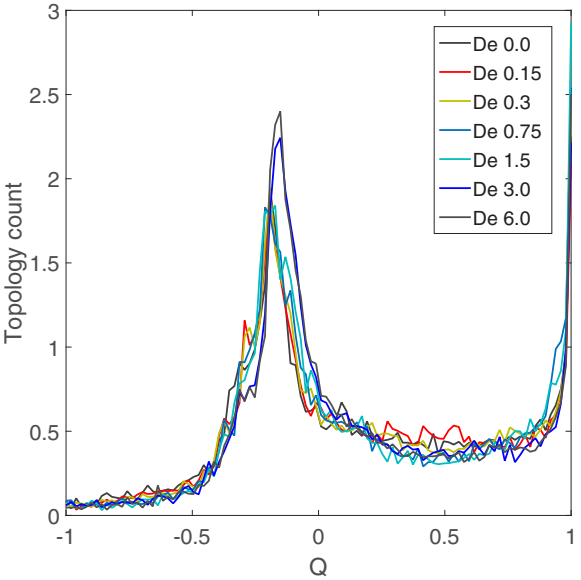

FIG. 14. Flow topology parameter histogram for the asymmetric configuration for different De.

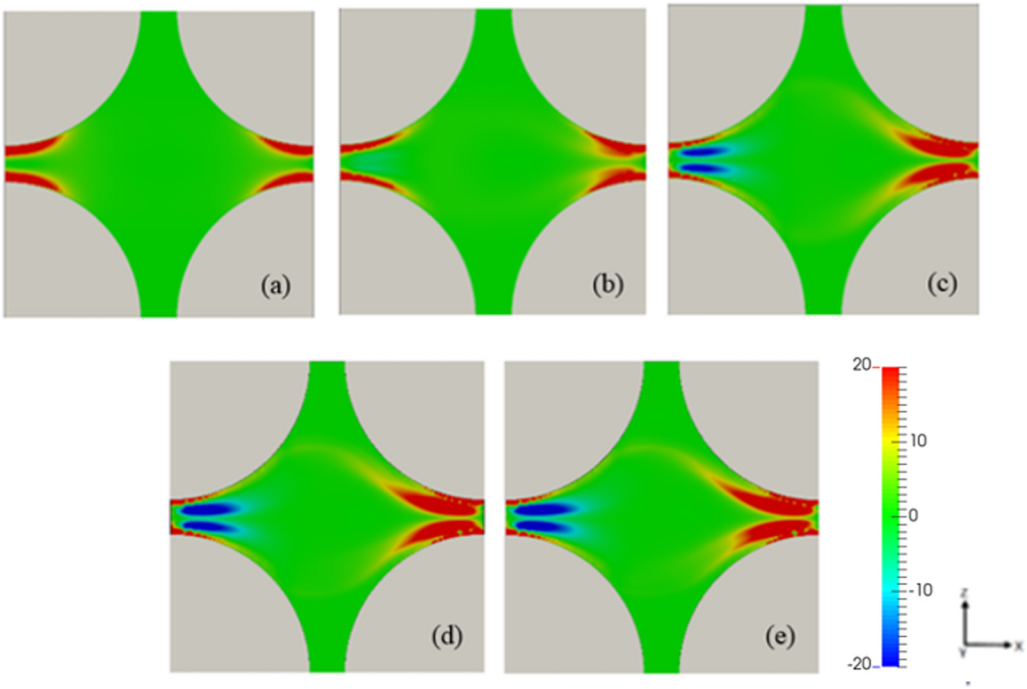

FIG. 15. Nondimensionalized work done by viscoelastic stresses at different De for the symmetric configuration: (a) De = 0.1, (b) De = 0.5, (c) De = 1.25, (d) De = 2.5, and (e) De = 5.0. The color range is clipped to clearly show regions of energy release at high De.

This can be understood to be a consequence of the more tortuous path in the asymmetric configuration leading to more pronounced rotational motion of the fluid. What is surprising is that in both cases this energy release is not taking place because of polymer coiling during relaxation of extensional flow ($Q = 1$), but rather because of polymer coiling during transitions from fast shear flow to slow shear flow.

We can observe from Figs. 17 and 18 that the nondimensionalized viscoelastic energy distribution rate decreases with increased De. This is explained by the fact that, as shown in Fig. 8, with increased De the fluid shear thins and thus the average velocity increases. This leads to a decrease in the nondimensional viscoelastic energy distribution rate per unit volume.

Up to this point we have focused on the work done by viscoelastic stresses. Next we analyze the total energy dissipation E_t, as a sum of viscoelastic and (Newtonian) solvent contributions, per unit volume. Figures 19 and 20 show the total work performed per unit fluid volume (and per unit Q) versus flow topology parameter in the entire flow domain for the symmetric and asymmetric configurations, respectively. Although the work of the viscoelastic stresses can be both positive and negative, energy is always dissipated from the Newtonian solvent contribution.

The total amount of nondimensional dissipated energy per unit volume (the integrals over Q in Figs. 19 and 20) decreases slightly with increasing De. This may be understood to be a consequence of the balance between energy fed into the system by the body force and energy removed by dissipation. Recall that in our simulations the relaxation time λ is varied while keeping the body force on the fluid constant. The amount of energy fed into the system per second therefore scales linearly with the (time-averaged) fluid flow rate. Dividing the (time-averaged) dissipated energy per second by the flow rate (volume per second) *once*, the amount of energy dissipated per unit volume of fluid flowing through the system must be independent of De. However, here we nondimensionalized

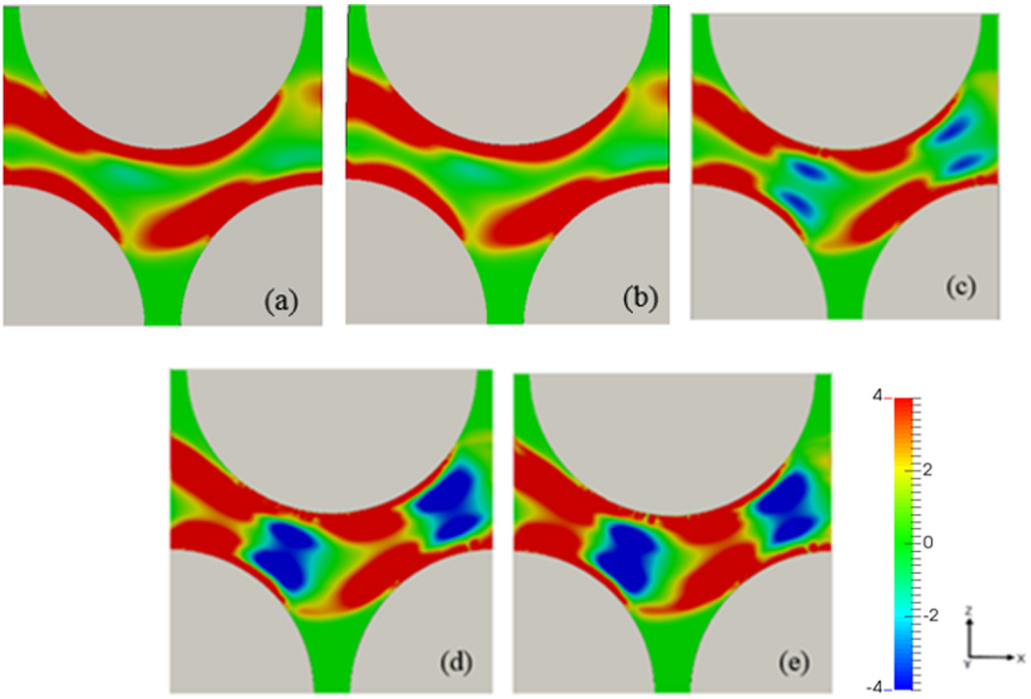

FIG. 16. Nondimensionalized work done by viscoelastic stresses at different De for the asymmetric configuration: (a) De = 0.15, (b) De = 0.3, (c) De = 1.5, (d) De = 3.0, and (e) De = 6.0. The color range is clipped to clearly show regions of energy release at high De.

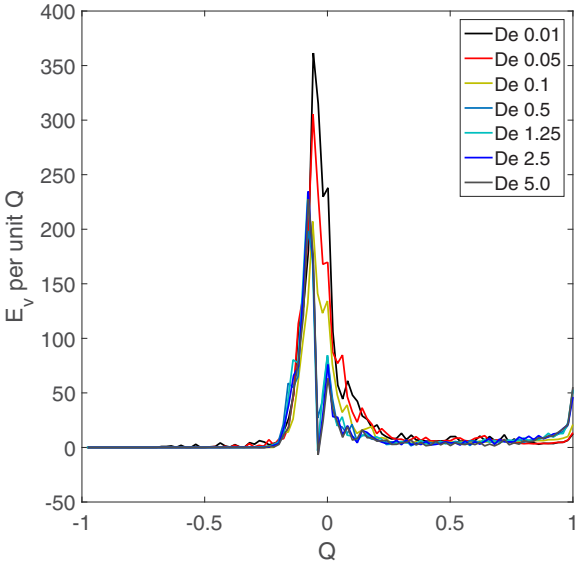

FIG. 17. Nondimensionalized viscoelastic energy distribution rate per unit volume (per unit Q) vs flow topology parameter Q in the symmetric configuration for different De.

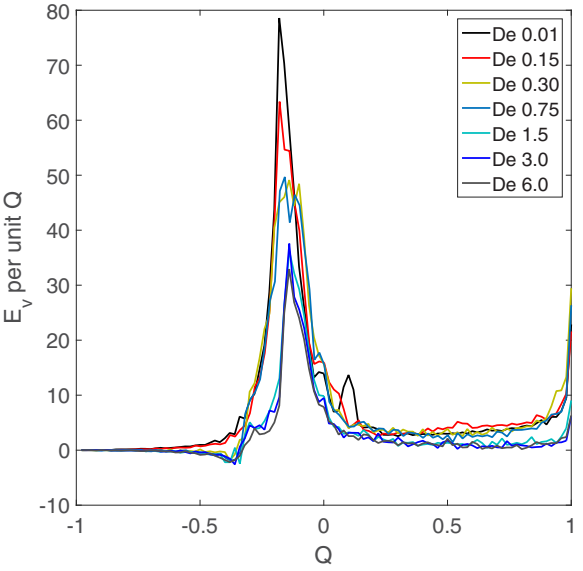

FIG. 18. Nondimensionalized viscoelastic energy distribution rate per unit volume (per unit Q) vs flow topology parameter Q in the asymmetric configuration for different De.

the results by dividing by the flow rate *twice*, so the increase in flow rate observed at larger De (inset in Fig. 8) results in a decrease in nondimensional energy dissipation.

Also observe that the typical magnitude of the total energy dissipation more or less doubles when comparing Figs. 17 and 18 to Figs. 19 and 20. This is in agreement with the value of β (0.33) used in this work, indicating similar contributions to the viscosity by the polymer and the solvent. From

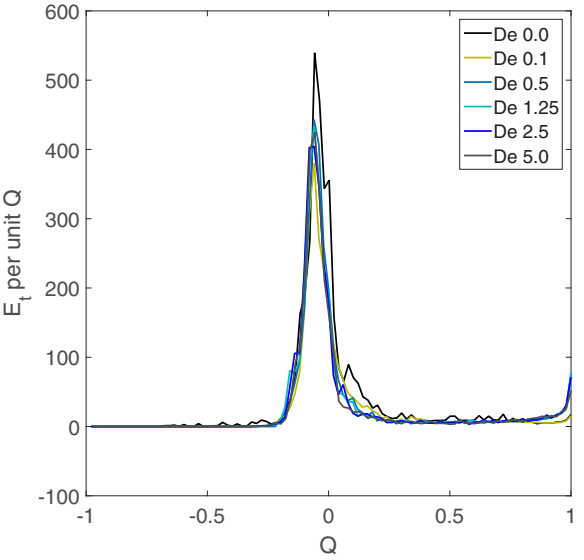

FIG. 19. Total (viscoelastic and solvent) nondimensional energy dissipation rate per unit volume (per unit Q) vs flow topology parameter Q in the symmetric configuration for different De.

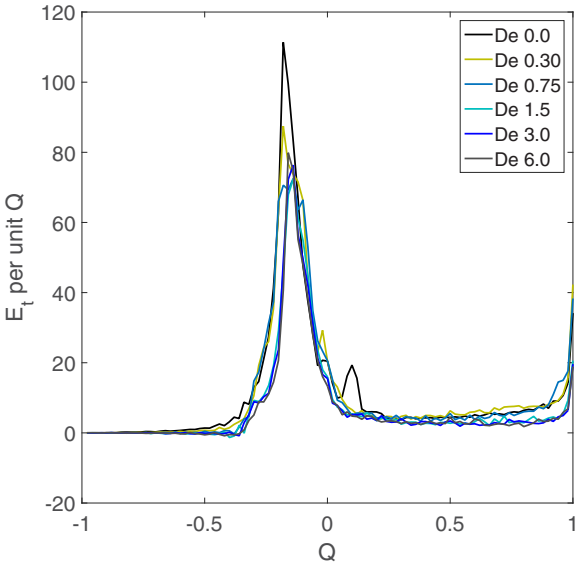

FIG. 20. Total (viscoelastic and solvent) nondimensional energy dissipation rate per unit volume (per unit Q) vs flow topology parameter Q in the asymmetric configuration for different De.

Figs. 19 and 20 it is evident that for both the symmetric and asymmetric configurations most of the total energy is dissipated in the shear-dominated regime.

In Fig. 21 we have characterized in detail the fraction of total energy dissipation caused by shear flow (Q in the range between $-1/3$ and $1/3$) and by elongation flow (Q in the range between $1/3$

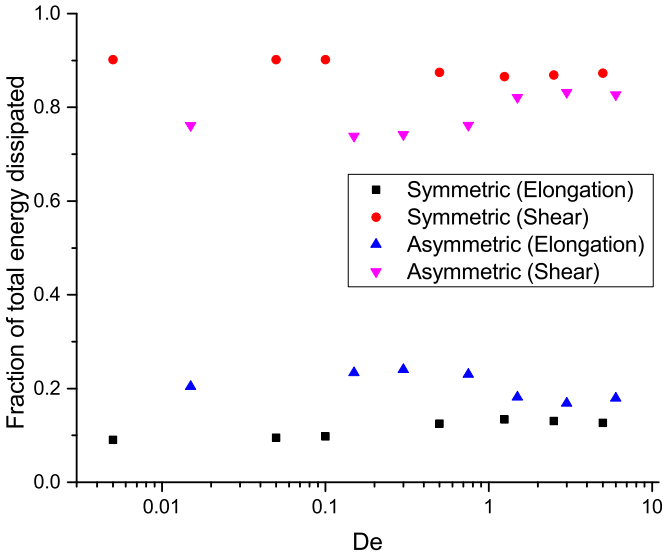

FIG. 21. Fractions of the rate of total (viscoelastic and solvent) energy dissipation, split between shear (Q between $-1/3$ and $1/3$) and elongation (Q between $1/3$ and 1) parts vs De for symmetric and asymmetric configurations. Note that the fraction of energy dissipation in the rotational (Q between -1 and $-1/3$) of the flow is always negligible.

and 1); we note that the fraction of energy dissipation in the rotational parts of the flow (Q between -1 and $-1/3$) is always negligible. The figure shows that in both the symmetric and asymmetric configurations the fractional contribution to the total energy dissipation by elongation flow is of the order of 10–20%. This confirms that also for the total energy dissipation, the shear flow is dominant. Note that for the asymmetric configuration, the elongational contribution (blue triangles) peaks at a De of the order of 1, i.e., it actually decreases again for larger De.

IV. CONCLUSION

We have applied a coupled finite-volume–immersed boundary method to study the flow of a viscoelastic fluid through two different model pore geometries with the same porosity. In agreement with the experiments of Rosales *et al.* [7], we observed that pore structure strongly affects the flow behavior for viscoelastic fluid flow. When the viscoelastic fluid passes through the symmetric and asymmetric arrangements of cylinders, due to difference in flow resistance, a different flow structure develops at higher viscoelasticity. Thus the apparent viscosities of the fluid at similar De are found to be largely different. A careful study of flow topology reveals how the different flow features, namely, rotation, shear, and extension, develop and change with increasing viscoelasticity. We have analyzed the viscoelastic work across the flow domain and tried to correlate between this work and flow topology for the two different flow domains. These analyses shed light on the complex interplay of fluid rheology and pore structures in a simplified model porous medium. The findings will facilitate a better understanding of viscoelastic fluid flow for more complex pore structures.

ACKNOWLEDGMENTS

This work was part of the Industrial Partnership Programme "Computational sciences for energy research" of the Foundation for Fundamental Research on Matter, which is part of the Netherlands Organisation for Scientific Research. This research program is cofinanced by Shell Global Solutions International B.V. The work was carried out on the Dutch national e-infrastructure with the support of SURF Cooperative.

[1] F. A. L. Dullien, *Porous Media-Fluid Transport and Pore Structure* (Academic, New York, 1979).
[2] D. F. James and D. R. McLaren, The laminar flow of dilute polymer solutions through porous media, J. Fluid Mech. **70**, 733 (1975).
[3] R. J. Marshall and A. B. Metzner, Flow of viscoelastic fluids through porous media, Ind. Eng. Chem. Fundam. **6**, 393 (1967).
[4] S. Rodriguez, C. Romero, M. L. Sargenti, A. J. Müller, A. E. Sáez, and J. A. Odell, Flow of polymer solutions through porous media, J. Non-Newtonian Fluid Mech. **49**, 63 (1993).
[5] C. Chmielewski and K. Jayaraman, Elastic instability in crossflow of polymer solutions through periodic arrays of cylinders, J. Non-Newtonian Fluid Mech. **48**, 285 (1993).
[6] K. Talwar and B. Khomami, Flow of viscoelastic fluids past periodic square arrays of cylinders: Inertial and shear thinning viscosity and elasticity effects, J. Non-Newtonian Fluid Mech. **57**, 177 (1995).
[7] F. J. G. Rosales, L. C. Deano, F. T. Pinho, E. V. Bokhorst, P. J. Hamersma, M. S. N. Oliveira, and M. A. Alves, Microfluidic systems for the analysis of viscoelastic fluid flow phenomena in porous media, Microfluid. Nanofluid. **12**, 485 (2012).
[8] P. C. Sousa, F. T. Pinho, M. S. N. Oliveira, and M. A. Alves, Efficient microfluidic rectifiers for viscoelastic fluid flow, J. Non-Newtonian Fluid Mech. **165**, 652 (2010).
[9] G. R. Moss and J. P. Rothstein, Flow of wormlike micelle solutions through a periodic array of cylinders, J. Non-Newtonian Fluid Mech. **165**, 1 (2010).

[10] J. R. A. Pearson and P. M. J. Tardy, Models for flow of non-Newtonian and complex fluids through porous media, J Non-Newtonian Fluid Mech. **102**, 447 (2002).
[11] T. Sochi, Pore-scale modeling of non-Newtonian flow in porous media, Ph.D. thesis, Imperial College London, 2007.
[12] A. W. Liu, D. E. Bornside, R. C. Armstrong, and R. A. Brown, Viscoelastic flow of polymer solutions around a periodic, linear array of cylinders: Comparisons of predictions for microstructure and flow fields, J. Non-Newtonian Fluid Mech. **77**, 153 (1998).
[13] D. Richter, G. Iaccarino, and E. S. G. Shaqfeh, Simulations of three-dimensional viscoelastic flows past a circular cylinder at moderate Reynolds numbers, J. Fluid Mech. **651**, 415 (2010).
[14] M. A. Hulsen, R. Fattal, and R. Kupferman, Flow of viscoelastic fluids past a cylinder at high Weissenberg number: Stabilized simulations using matrix logarithms, J. Non-Newtonian Fluid Mech. **127**, 27 (2005).
[15] L. Skartsis, B. Khomani, and J. L. Kardos, Polymeric flow through fibrous media, J. Rheol. **36**, 589 (1992).
[16] F. J. Alcocer and P. Singh, Permeability of periodic arrays of cylinders for viscoelastic flows, Phys. Fluids **14**, 2578 (2002).
[17] A. F. Morais, H. Seybold, H. J. Herrmann, and J. S. Andrade, Jr., Non-Newtonian Fluid Flow Through Three-Dimensional Disordered Porous Media, Phys. Rev. Lett. **103**, 194502 (2009).
[18] J. J. J. Gillissen, Viscoelastic flow simulations through an array of cylinders, Phys. Rev. E **87**, 023003 (2013).
[19] M. Grilli, A. Vázquez-Quesada, and M. Ellero, Transition to Turbulence and Mixing in a Viscoelastic Fluid Flowing Inside a Channel with a Periodic Array of Cylindrical Obstacles, Phys. Rev. Lett. **110**, 174501 (2013).
[20] E. S. G. Shaqfeh, Purely elastic instabilities in viscometric flows, Annu. Rev. Fluid Mech. **28**, 129 (1996).
[21] G. H. McKinley, W. P. Raiford, R. A. Brown, and R. C. Armstrong, Nonlinear dynamics of viscoelastic flow in axisymmetric abrupt contractions, J. Fluid Mech. **223**, 411 (1991).
[22] L. Pan, A. Morozov, C. Wagner, and P. E. Arratia, Nonlinear Elastic Instability in Channel Flows at Low Reynolds Numbers, Phys. Rev. Lett. **110**, 174502 (2013).
[23] P. Pakdel and G. H. McKinley, Elastic Instability and Curved Streamlines, Phys. Rev. Lett. **77**, 2459 (1996).
[24] A. Groisman and V. Steinberg, Elastic turbulence in a polymer solution flow, Nature (London) **405**, 53 (2000).
[25] A. Groisman and V. Steinberg, Mechanism of elastic instability in Couette flow of polymer solutions: Experiment, Phys. Fluids **10**, 2451 (1998).
[26] R. G. Larson, E. S. Shaqfeh, and S. J. Muller, A purely elastic instability in Taylor-Couette flow, J. Fluid Mech. **218**, 573 (1990).
[27] Y. L. Joo and E. S. Shaqfeh, A purely elastic instability in Dean and Taylor-Dean flow, Phys. Fluids A **4**, 524 (1992).
[28] R. G. Larson, Instabilities in viscoelastic flows, Rheol. Acta **31**, 213 (1992).
[29] H. Yatou, Flow pattern transition accompanied with sudden growth of flow resistance in two-dimensional curvilinear viscoelastic flows, Phys. Rev. E **82**, 036310 (2010).
[30] S. De, S. Das, J. A. M. Kuipers, E. A. J. F. Peters, and J. T. Padding, A coupled finite volume immersed boundary method for simulating 3D viscoelastic flows in complex geometries, J. Non-Newtonian Fluid Mech. **232**, 67 (2016).
[31] R. B. Bird, R. C. Armstrong, and O. Hassager, *Dynamics of Polymeric Liquids*, 2nd ed. (Wiley, New York, 1987), Vol. 1.
[32] J. L. Favero, A. R. Secchi, N. S. M. Cardozo, and H. Jasak, Viscoelastic flow analysis using the software OpenFOAM and differential constitutive equations, J. Non-Newtonian Fluid Mech. **165**, 1625 (2010).
[33] R. Guénette and M. Fortin, A new mixed finite element method for computing viscoelastic flows, J. Non-Newtonian Fluid Mech. **60**, 27 (1995).

[34] See Supplemental Material at http://link.aps.org/supplemental/10.1103/PhysRevFluids.2.053303 for viscoelastic flow simulations in a model porous medium.

[35] D. F. James, R. Yip, and I. G. Currie, Slow flow of Boger fluids through model fibrous porous media, J. Rheol. **56**, 1249 (2012).

[36] C. E. Wagner and G. H. McKinley, The importance of flow history in mixed shear and extensional flows, J. Non-Newtonian Fluid Mech. **233**, 133 (2016).